Title

Desolvated cations promote CO electroreduction through partial covalent interactions

Journal

NATURE CATALYSIS

ISSN

2520-1158

Authors

Shan, Yu
Jaugstetter, Maximilian
Feijoo, Julian
et al.

Publication Date

2026-08-31

DOI

10.1038/s41929-026-01604-w

Desolvated cation promotes CO_2 electroreduction through partial covalent interaction

Authors List

Yu Shan[1, 2, †], Maximilian Jaugstetter[1, †], Julian Feijoo[1, 3, †], Yani Guan[4, †], Tianle Wang[1, 3], Lorenz J. Falling[1], Jialu Li[5], Honghe Ding[5], Alex Sachelarie[3], Maria Fonseca Guzman[1, 3], Xiao Zhao[2], Robert Michael Kowalski[4], Slavomír Nemšák[5, 6], Jinghua Guo[5, 7], Philippe Sautet[4, 8, *], Miquel B. Salmeron[1, 2, *] and Peidong Yang[1, 2, 3, 9, *]

Affiliations

[1] Chemical Sciences Division, Lawrence Berkeley National Laboratory; Berkeley, California, 94720, United States

[2] Department of Materials Science and Engineering, University of California at Berkeley; Berkeley, California 94720, United States

[3] Department of Chemistry, University of California at Berkeley; Berkeley, California 94720, United States

[4] Department of Chemical and Biomolecular Engineering, University of California Los Angeles, Los Angeles, California 90095, United States

[5]Advanced Light Source, Lawrence Berkeley National Laboratory; Berkeley, California, 94720, United States

[6]Department of Physics and Astronomy, University of California, Davis, CA 95616, United States

[7]Department of Chemistry and Biochemistry, University of California, Santa Cruz, CA 95064, United States

[8]Department of Chemistry and Biochemistry, University of California Los Angeles, Los Angeles, California 90095, United States

[9]Kavli Energy NanoScience Institute, Berkeley, CA 94720, USA.

†These authors contributed equally to this work.

*Corresponding author. Email: sautet@ucla.edu, mbsalmeron@lbl.gov, p_yang@berkeley.edu

Abstract

Cations play a critical role in electrochemical CO_2 reduction, yet the mechanisms underlying their influence remain poorly understood due to limited knowledge of their solvation structures and interfacial interactions under operating conditions. Here, we combine surface-sensitive total electron yield X-ray absorption spectroscopy (TEY-XAS), surface-enhanced infrared absorption spectroscopy (SEIRAS), and density functional theory (DFT) calculations to determine the solvation environment of cesium ions near a ligand-modified silver nanocatalyst under CO_2-reducing conditions. We find that desolvated Cs^+ ions, confined between a floating ligand layer and the silver surface, enable CO_2 activation at potentials as high as 0.4 V versus RHE—reducing the overpotential for CO_2-to-CO conversion by 250 mV compared to a bare Ag film. Our results further reveal a partial covalent character in Cs–intermediate interactions, which directly accounts for the enhanced catalytic activity. These findings provide multimodal spectroscopic evidence of desolvated cations and demonstrate their ability to interact with surface-bound species, engaging in partial charge transfer and thereby modulating reaction kinetics beyond purely electrostatic effects. This work offers a unified mechanism for cation-mediated catalysis and presents a promising strategy for designing next-generation electrochemical systems with reduced energy demands.

Introduction

Renewable energy-powered electrochemical CO_2 reduction (CO_2R) has emerged as a promising approach to mitigate anthropogenic carbon emissions and reduce reliance on fossil fuels by producing fuels and chemical feedstocks[1,2]. The ultimate goal of CO_2R is to achieve high selectivity toward desired products while minimizing energy input, typically reflected by lower overpotential. In addition to the choice of transition metal electrocatalysts, which are commonly employed for CO_2R, the electrolyte composition—particularly the identity of the cation—can significantly influence both the energy efficiency and product distribution of the reaction[3,4]. The effect of cations in CO_2R has been extensively studied, and several key observations have been consistently reported across various catalyst types and cell configurations. First, the presence of alkali metal cations is essential for the occurrence of CO_2R, particularly in H-cell systems, where interfacial electric field is relatively weak[5,6]. Second, CO_2R catalytic activity correlates with the radius of the alkali cation: $Cs^+ > K^+ > Na^+ > Li^+$[7-10].

While the critical role of cations in CO_2R is widely recognized, and the trend above has been consistently observed regardless of catalyst identity, morphology, or cell configuration, the underlying mechanisms behind the observed cation-dependent activity trend remain under debate. Broadly, four main hypotheses have been proposed: larger, weakly hydrated cations (e.g., Cs^+) (1) induce a stronger near-surface electric field[11,12]; (2) decrease the pKa of cation hydrolysis and thus provide better buffering capacity at the interface[9,13]; (3) partially shed their solvation shells and stabilize key CO_2R intermediates through electrostatic interactions[14-17]; and (4) accelerate the hydrogenation of intermediates in acidic conditions[6]. These hypotheses are primarily supported by theoretical simulations, while direct experimental evidence remains limited and often fails to reflect realistic catalytic operating conditions. Furthermore, these explanations are not mutually exclusive—they are essentially different manifestations of the same phenomenon: the solvation properties of cations and their interfacial behavior under CO_2-reducing conditions. Therefore, to comprehensively explain cation effects in CO_2R, one must combine complementary techniques capable of probing various facets of cation solvation and track their evolution under *operando* conditions in real catalytic systems.

Recently, our group developed a catalytic architecture called the nanoparticle-ordered ligand interlayer (NOLI), which exhibits benchmark CO_2 conversion activity[18,19]. For example, Ag/Au NOLI achieves 100% Faradaic efficiency (FE) toward CO at −0.78 V_{RHE} and −0.40 V_{RHE}, respectively[18]; Pd NOLI achieves 100% formate FE at −0.20 V_{RHE}[18]; and Cu NOLI reaches over 55% FE toward C_{2+} products at −0.85 V_{RHE}[19]. In the NOLI system, cations are confined in an aqueous layer sandwiched between a detached, ordered ligand layer and the negatively charged metal surface[18,20]. Notably, once the ligand layer is intentionally removed after NOLI formation, the catalytic performance collapses, despite preservation of nanoparticle size, morphology, and crystallinity. This result demonstrates that the ligand-defined interfacial environment—rather than the metallic scaffold itself—is responsible for the enhanced catalytic performance. Consistent with one of the proposed mechanisms, the *ab initio* molecular dynamics (AIMD) simulations suggest that cations entering this environment partially shed their solvation shells and stabilize key CO_2R intermediates[18]. Importantly, we observe the same cation-dependent trend in NOLI systems across different metallic catalyst, with Cs^+ consistently enhancing CO_2R the most (Supplementary Fig.1). Even more intriguingly, for every alkali cation, NOLI shifts the performance profile by approximately 200 mV toward lower overpotentials compared to its metal thin film counterpart, suggesting that the cation effect is significantly amplified in NOLI. This makes the NOLI architecture an ideal platform to study cation solvation structures and their relationship with CO_2R activity, as it both preserves and enhances the traditional cation trend—thereby increasing the likelihood of observing solvation structure changes.

In this work, using Ag-NOLI as a representative system, we utilized a combination of surface-sensitive vibrational and X-ray spectroscopies to investigate the solvation structure of Cs^+ and its influence on CO_2 reduction. *In situ* attenuated

total reflection surface-enhanced infrared absorption spectroscopy (ATR-SEIRAS) unveils that at the solid-liquid interface of Ag NOLI, the floating ligand layer maintains a highly confined, ion-rich microenvironment where CO_2 activation is facilitated by desolvated Cs^+ at a potential as high as 0.4 V_{RHE}, a process that accounts for the superior catalytic activity of NOLI. Concurrently, *in situ* electron yield X-ray absorption spectroscopy (XAS) at the O K-edge and Cs M-edge demonstrates that the promotional effect of desolvated cations originates from direct interactions with adsorbed $*CO_2$. Notably, further DFT-assisted analysis of the Cs M-edge spectra reveals that the Cs–CO_2 interaction exhibits partial covalent character. These findings suggest that Cs^+ not only stabilizes reaction intermediates electrostatically but also participates in partial orbital hybridization, thereby substantially influencing reaction kinetics. Altogether, this work provides direct spectroscopic evidence for the presence and reactivity of desolvated cations and uncovers a previously underappreciated mechanism of cation–intermediate interaction. By linking distinct mechanisms about cation effects to a unified origin rooted in cation solvation structure, our results establish ligand-enabled interfacial confinement as a generalizable design principle for catalytic systems aiming to leverage cation reactivity.

Results

Ligand-modulated ionic environment facilitates CO_2 adsorption.

The CO_2R performance of two silver-based systems—Ag foil and Ag NOLI—are presented in Fig. 1a and 1b. As expected, both systems exhibit a cation-dependent enhancement in activity and selectivity. In the Ag NOLI system, CO FE increases from 42% in 0.1 M $NaHCO_3$ to 79% in $KHCO_3$, and further to 85% in $CsHCO_3$ at –0.68 V_{RHE}. A similar trend is observed for Ag foil, though with much lower absolute values: CO selectivity increases from 2% to 10% and 12% under the same electrolyte conditions. All reported potentials in this work are referenced to the reversible hydrogen electrode (RHE), unless otherwise noted. In both systems, the partial current density for CO production also increases with cation size, from Na^+ to Cs^+. Notably, the NOLI system shows a dramatic improvement in both selectivity and activity compared to the Ag foil, regardless of the cation identity. This enhancement highlights the significant promotional effect of the NOLI architecture on CO_2R.

The performance enhancement associated with NOLI is not exclusive to silver. As shown in Supplementary Fig.1, similar improvements are observed for Cu and Au NOLI systems compared to their corresponding single crystal counterparts, suggesting that the catalytic boost conferred by the NOLI structure is generalizable across different metals. While copper is widely recognized for its unique ability to catalyze the formation of multi-carbon products from CO_2 at appreciable rates, its susceptibility to structural and chemical transformations under electrochemical bias, along with its complex reaction pathways, complicates the study of cation solvation structures[2,21]. In contrast, silver offers greater stability under applied potentials and features a simpler, better-understood CO_2-to-CO conversion pathway. Therefore, in this work, Ag NOLI was chosen as the model system for studying the cation solvation structure and its influence on CO_2R. We believe that the conclusions drawn from this work may be applied to other heterogeneous electrocatalytic systems.

To elucidate how the NOLI architecture promotes CO_2 reduction at low overpotentials, *in situ* ATR-SEIRAS measurements were performed using 0.1 M $CsHCO_3$ as the electrolyte. The schematic of the *in situ* ATR-SEIRAS cell is shown in Supplementary Fig. 2. Prior to spectral collection, the electrode was preconditioned by a linear sweep voltammetry (LSV) from open-circuit potential (OCV, around 0.6V_{RHE}) to –0.8 V_{RHE}, followed by stabilization at –0.8 V_{RHE} for at least 10 minutes. This preconditioning step induces ligand detachment and the aggregation of small Ag

nanoparticles into larger polycrystalline domains, establishing the NOLI structure (Supplementary Figs. 3-4). A detailed discussion of changes of the interfacial microenvironment during this preconditioning process is provided in the Supplementary Discussion 1. The successful formation of NOLI was confirmed by observing the dynamic attraction/repelling behavior of the ligands in response to applied bias (Supplementary Fig.6).

After NOLI formation, the electrode was rested at OCV for 30 minutes under continuous CO_2 bubbling to remove surface-adsorbed species formed during preconditioning. The IR spectrum at this state was used as a reference for all subsequent spectra. Fig. 1c and 1d present SEIRAS spectra of the fingerprint region (1200–2200 cm^{-1}) and water stretch region (3000–3800 cm^{-1}) under increasingly negative biases. A feature at 1372 cm^{-1} emerges around 0.4 V_{RHE}, reaches maximum intensity near 0.1 V_{RHE}, and then gradually decreases with further negative bias, disappearing entirely around –0.2 V_{RHE}, while shifting slightly to 1362 cm^{-1}. Following the disappearance of this feature, a new peak around 1846 cm^{-1} appears, accompanied by an increasingly negative band at 1232 cm^{-1}. Based on our previous work[20], the 1232 cm^{-1} band is assigned to the ν(P=O) vibration of tetradecylphosphonic acid (TDPA) ligands (see Supplementary Discussion 1), where the negative signal indicates ligands moving further away from the Ag surface.

Additionally, a peak around 1990 cm^{-1} is observed from –0.4 V_{RHE} to –0.8 V_{RHE}, shifting to lower wavenumbers as the bias becomes more negative. By –0.8 V, the 1846 cm^{-1} and 1990 cm^{-1} features shift to 1804 cm^{-1} and 1966 cm^{-1}, respectively. The observed Stark shifting behavior strongly suggests that these modes correspond to surface-adsorbed species. We assign these two modes to bridge-adsorbed ($*CO_B$) and linearly adsorbed ($*CO_L$) CO species, respectively, which aligns well with literature reported IR frequencies of CO adsorbed on Ag surfaces[22-24]. This assignment is further supported by the observation that these bands increase in intensity over time when CO_2 is reintroduced into a N_2-saturated 0.1 M $CsHCO_3$ electrolyte at –0.8 V_{RHE} (Supplementary Fig.7), indicating that they are intermediates of CO_2 reduction rather than surface-bound hydrogen, which has also been reported in this spectral window[25]. Notably, bridge-bonded *CO is typically favored at low CO coverage on Ag, while $*CO_L$ becomes dominant at higher coverage[26], consistent with our observation that the 1846 cm^{-1} feature appears first at lower overpotentials. This behavior rules out the possibility of *CO adsorbed on Pt—a common source of contamination in SEIRAS—since Pt favors atop-bound CO at low coverages[27-29]. Although both bridge- and linear-bound CO species are observed, CO-induced site blocking is unlikely under the present conditions. CO is generated only *in situ* at very low partial pressures (~6×10^{-4} atm), far below the regime where competitive CO/CO_2 adsorption has been reported[30].

The nature of the 1372 cm^{-1} feature was further investigated. Given the potential-dependent shift of this vibrational mode, it is most likely associated with a surface-bound species. While vibrational modes associated with (bi)carbonate species are commonly observed in this spectral region[31], such an assignment appears unlikely in our system. Adsorbed $*HCO_3^-$/$*CO_3^{2-}$ would be expected to detach under increasingly negative potentials, leading to a progressively negative peak rather than the observed buildup and decay. To probe whether this feature involves hydrogen, ATR-SEIRAS measurements were repeated in 0.1 M $CsDCO_3$ (in D_2O), as vibrational modes involving hydrogen typically experience redshift when hydrogen is replaced by deuterium[6]. No significant shift was observed in the D_2O spectra (Supplementary Fig.8), indicating that the 1362 cm^{-1} mode does not involve hydrogen. Given that the appearance and disappearance of this feature coincide with the emergence of *CO adsorption, we propose that the 1362 cm^{-1} band corresponds to the symmetric O–C–O stretch (ν_s(O–C–O)) of an adsorbed CO_2 intermediate. The asymmetric stretch, typically expected around 1500 cm^{-1}, is not observed due to the surface selection rules of SEIRAS[6,32,33]. Importantly, adsorption of CO_2 on metal surfaces requires activation of the linear molecule through bending, which lifts the degeneracy of the $2\pi_u$ LUMO and enables hybridization with metal states. This interaction necessarily involves partial electron transfer from the metal into the CO_2 antibonding orbital, yielding a bent adsorbate with partial negative

charge[5,16]. Therefore, the observed 1372 cm^{-1} feature is less likely to correspond to a charge-neutral adsorbed CO_2 species. Instead, we assign it to (partially) reduced CO_2, denoted $*CO_2^-$ or activated CO_2 in the following discussion.

In addition to carbon-related intermediates, changes in water-related modes were also observed. In the fingerprint region (Fig. 1c), the H–O–H bending mode shows a negative feature around 1620 cm^{-1} that becomes more prominent under negative biases. New features at 1600 cm^{-1} and 1660 cm^{-1} gradually build up as the potential becomes more negative. In the OH stretching region (Fig. 1d), the negative band at 3580 cm^{-1} becomes more intense at moderate biases and then partially recovers at higher negative potentials, accompanied by intensity increases at 3200–3400 cm^{-1}. Similar effects are reproduced in OD stretching mode in 0.1M $CsDCO_3$ (Supplementary Fig.9). The synchronous evolution of the 1620 and 3580 cm^{-1} features suggests they belong to the same water species. Notably, the 1620 and 3580 features have been observed in ATR-IR spectra of highly concentrated electrolytes (~10 M), where their intensity scales with ion concentration (Supplementary Fig.10). Therefore, these bands are assigned to water molecules tightly associated with the solvation shell of cations, which is consistent with multiple spectroscopic studies on interfacial water structure[34-36].

The integrated band intensities of the vibrational modes detected in Fig. 1c and 1d at different applied potentials are summarized in Fig. 1e. In the potential window from OCV to –0.2 V_{RHE}, the increasing negative area associated with H_2O in the cation solvation shell with increasingly negative potentials indicates progressive cation desolvation, i.e. reduction of the number of water molecules coordinated to the cation. Interestingly, activated $*CO_2$ is also observed within this same potential window, notably more positive than the potentials typically reported for $*CO_2$ activation on Cu[6,37]. The simultaneous occurrence of these two phenomena suggests that CO_2 activation at such low overpotentials is facilitated by desolvated cations. As illustrated schematically in Fig. 1f, within this potential range, $*CO_2$ molecules replace the H_2O molecules originally present in the cation solvation shell. The displaced water molecules reorganize into a bulk-like phase with a strong hydrogen-bond network, which explains the intensity increase observed between 3200–3400 cm^{-1} in Fig. 1d—a spectral signature characteristic of strongly hydrogen-bonded, bulk-like water.

Notably, *CO species only appear when the applied potential becomes more negative than –0.2 V_{RHE} , coinciding with the disappearance of the $*CO_2^-$ signal. This observation suggests that the rate-determining step (RDS) for CO formation is the generation of $*CO_2^-$ via the first electron-transfer activation step, rather than the subsequent conversion of $*CO_2^-$ to *CO. Interestingly, the emergence of *CO also coincides with the recovery of water-related vibrational bands (Fig. 1e), which might initially imply that protons or water molecules participate in the RDS. However, as shown in Supplementary Fig.11, the CO partial current density (j_{CO}) is nearly identical in both deuterated and protic electrolytes, indicating that proton transfer does not contribute to the rate-determining step. Together, these findings support a mechanism in which CO_2 activation proceeds via an electron-transfer-coupled adsorption step facilitated by desolvated cations:

$$CO_2 + * + M^+ + e^- \rightarrow *CO_2^- \cdots M^+$$

which constitutes the RDS for CO formation. The observed recovery of water-related signals is therefore attributed to further ligand detachment at –0.2 V_{RHE} or more negative potentials, which enables increased water access to the interfacial region, rather than indicating a direct role of water in the RDS of *CO formation.

The production of gaseous CO on Ag NOLI is first detected around –0.4 V_{RHE} (Fig. 1b), a potential where $*CO_L$ starts to be observed, suggesting that a critical surface coverage of CO must be reached before desorption occurs. To elucidate the origin of the promotion effect of CO_2 activation in the NOLI architecture, SEIRAS spectra were also collected for a ligand-free Ag film. As shown in Supplementary Fig.12, under negative bias, the negative band associated with H_2O

stretching is nearly absent, indicating that the interfacial cations remain more solvated than in the NOLI system under equivalent potentials. Moreover, no discernible $*CO_2$-related features appear across the scanned potential range, likely due to lower $*CO_2^-$ surface coverage compared to Ag NOLI. Consequently, the onset potentials for both $*CO_B$ and $*CO_L$ species on the Ag film are at least 250 mV more negative than those observed in Ag NOLI. This comparison highlights that CO_2 activation is significantly facilitated by desolvated cations within the NOLI architecture.

Results from *in situ* SEIRAS clearly reveal the promotional effect of desolvated cations on $*CO_2$ activation in Ag NOLI. To determine whether this enhancement arises primarily from an enhanced interfacial electric field generated by desolvated cations or from direct stabilization of reaction intermediates, we probed the Stark tuning behavior of adsorbed $*CO_L$ to assess the interfacial electric field of Ag NOLI (see Supplementary Discussion 2 for details). As shown in Supplementary Fig.13, within the potential range where $*CO_2^-$ is observed (0.4 V_{RHE} to –0.2 V_{RHE}), the vibrational Stark tuning rate of $*CO_L$ is approximately 8 cm^{-1} V^{-1}, which is substantially smaller than the ~30 cm^{-1} V^{-1} typically reported for *CO on metal films[7,37-39]. This comparison indicates that the local electric field in this potential window is relatively modest and allows us to exclude mechanisms based solely on amplified interfacial electric fields. Instead, these results point toward a mechanism in which direct interactions between desolvated Cs^+ ions and adsorbed $*CO_2^-$ intermediates play a decisive role in promoting this activation—a hypothesis that will be further examined in the following sections.

Interactions within the water-deficient NOLI pocket

To elucidate the interactions between desolvated Cs^+ and interfacial species in Ag-NOLI, *in situ* X-ray absorption spectroscopy (XAS) was employed. Interface-sensitive information was obtained using total electron yield (TEY) detection. Fig. 2a schematically illustrates the liquid flow cell configuration used for the XAS measurements in this study. In this liquid-cell geometry, X-ray absorption at the solid–liquid interface creates a core hole. Core-hole relaxation generates Auger electrons, whose kinetic energies are determined by atomic energy levels. These Auger electrons undergo inelastic scattering in the surrounding aqueous medium and generate cascades of low-energy secondary electrons[40]. Owing to the short mean free path of these electrons in aqueous media, only those generated within a few nanometers of the electrode can reach the conductive surface and be collected as a photoinduced current before recombining with ionized species in the electrolyte[41,42]. This photoinduced current (the TEY signal) follows the X-ray absorption cross section and is used to reconstruct the XAS spectra. Further experimental details provided in the Materials and Methods section.

We first focus on the oxygen K-edge XAS spectra, as it is well-established for characterizing aqueous systems[43,44]. In condensed phases, water typically exhibits three distinct spectral features: a pre-edge near 535.0 eV, a main edge near 537.5 eV, and a post-edge near 541.0 eV. The pre-edge intensity scales with the asymmetry in local molecular environment, while the post-edge scales with the number of H-bonds[45-48]. For example, liquid water displays a strong pre-edge and subtle post-edge, while ice shows a more subtle pre-edge and more pronounced post-edge. As shown in Fig. 2b, the interfacial water structure near a thin silver film exhibits minimal changes from pure water to 0.5 M $CsHCO_3$; only a slight increase in the pre-edge intensity is observed, likely due to the structure-breaking nature of Cs^+ cations[9]. In contrast, Ag NOLI displays markedly different behavior (Fig. 2c). Before preconditioning, when ligands are covalently attached to the Ag surface, water is excluded from the surface by the hydrophobic alkyl chains of the ligands. In this initial state, the phosphonic acid headgroup is expected to be the only oxygen-containing species detectable near

the surface (Supplementary Fig.3). Indeed, the absence of interfacial water at OCV is evident from the spectrum, which shows a strong peak at 535.2 eV and a weaker second peak at 536.9 eV, an intensity trend that is opposite to that of water. We assign this spectrum to TDPA molecules chemisorbed onto the Ag nanoparticle surface via a bidentate configuration[20]. Dry TDPA powder exhibits a similar spectrum; minor differences can be ascribed to the different protonation state of the headgroup[49].

After applying a bias of –0.8 V_{RHE} for 10 minutes to induce NOLI formation and then returning to OCV (around 0.6 V_{RHE}), the oxygen K-edge XAS spectrum changes drastically to resemble that of water, indicating the formation of an aqueous pocket at the interface (Fig. 2c) after preconditioning. Upon applying a potential of 0.4 V_{RHE} —close to the onset of $*CO_2^-$ adsorption as shown in Fig. 1e—the O K-edge spectrum undergoes another dramatic shift, reverting to a shape similar to that of pure TDPA. Almost no intensity remains near water's main and post-edge features, indicating that a significant amount of the water previously confined within the NOLI pockets at OCV has been expelled further from the surface at 0.4 V_{RHE}, leading to the formation of a highly water-deficient environment populated by desolvated Cs^+ cations. This observation is consistent with SEIRAS measurements, where the OH stretching bands show negative features under 0.4 V_{RHE}. The highly ionic environment decreases the Debye length and rapidly screens the negative charge at the interface, allowing the ligands to settle closer to the surface. Compared to chemisorbed TDPA (the OCV spectrum before precondition), the peak maximum at 0.4 V_{RHE} appears slightly red-shifted. A similar red-shift has been observed in first-principles XAS simulations for the protonation of sulfate species[50], leading us to propose that protonation of the phosphonic acid headgroup following ligand detachment is responsible for the red-shift observed here[20], although contributions from interactions with other interfacial species cannot be ruled out.

When applying an even more negative bias of 0.2 V_{RHE}, a more water-deficient spectrum is obtained. Interestingly, the peak maximum continues to red-shift, and a new broad pre-peak emerges at ~528.8 eV—a feature that is absent in both pure TDPA and pure water spectra. To further investigate this signature, we prepared a Cs-TDPA compound where oxygen atoms of the phosphonic acid headgroup are interacting with a Cs cation (Fig. 2c). The spectrum of this compound matches well with that of the 0.2 V_{RHE} spectrum, with a pronounced shoulder around 528.8 eV (Fig. 2c), This finding suggests a direct interaction between the TDPA head group and Cs^+ at 0.2 V_{RHE}.

Together, the *in situ* XAS and ATR-SEIRAS results demonstrate that under moderate bias, the NOLI pocket becomes a highly confined, water-deficient interfacial environment dominated by desolvated cations, detached ligands, and surface intermediates. In this microenvironment, Cs^+ not only sheds its hydration shell but also directly interacts with detached ligands. However, O K-edge spectra alone do not provide direct information on Cs–intermediate interactions. To probe these interactions, we next turned to *in situ* XAS at the Cs M-edge.

Interpretation of Cs M edge spectra

Recent work has demonstrated that *in situ* XAS at alkali-metal edges can directly capture electronic structure changes of cations induced by interactions with adsorbed reaction intermediates[51], motivating the use of Cs M-edge XAS to directly interrogate Cs–intermediate coupling under operando CO_2 reduction conditions. To develop a fundamental understanding of the behavior of the largely unexplored Cs M-edges, we first measured several relevant reference samples. Fig. 3a presents the Cs M_4 and M_5 edges of solid-state Cs_2CO_3, $CsHCO_3$, and CsI. These absorption features arise from electronic transitions from the 3d core level to the unoccupied 4f orbitals, with the two main absorption edges resulting from spin–orbit coupling of the 3d core hole. Interestingly, additional satellite features are observed at

relatively higher energies—specifically at ~742.5 eV and ~757.0 eV. The intensity of these satellite features is highest in Cs_2CO_3, weaker in $CsHCO_3$, and barely visible in CsI.

A similar trend has been reported by Osaka et al., who observed prominent satellite structures in vermiculite (a mineral containing Cs and O), but much weaker features in cesium halides[52]. They attributed the appearance of these satellites to the formation of delocalized 4f orbitals via hybridization between Cs 4f and anion orbitals. While Cs 4f orbitals exhibit minimal overlap with halide orbitals, they strongly interact with O 2p orbitals, explaining the more pronounced tail structures in oxygen-containing compounds. Notably, comparable behavior has also been observed in M-edge spectra of lanthanide oxides, where similar satellite features arise from hybridization between lanthanide 4f orbitals and O 2p orbitals[53]. Together, these findings suggest that the satellite intensities in our Cs M-edge spectra reflect the degree of orbital mixing between Cs 4f and neighboring anion orbitals. In addition, they also indicate that beyond the pure electrostatic effect, Cs and O form a partial covalent bond in $CsHCO_3$ and Cs_2CO_3.

Although the M-edge tail structure provides insight into the local coordination environment of the unoccupied 4f orbitals, the 4f orbitals in Cs^+ are largely empty in the ground state. To assess whether Cs M-edge features reflect broader ground-state interactions, we therefore combined density of states (DOS) calculation, Bader charge analysis, differential charge density (ΔQ), and electron localization function (ELF) calculations for Cs_2CO_3, $CsHCO_3$, and CsI. As shown in Fig. 3b, the density of states (DOS) reveals that Cs 5s and 5p orbitals lie within the energy ranges of –20 to –25 eV and –5 to –10 eV, respectively. In CsI, no orbital overlap is observed, and orbitals show no dispersion, indicating purely ionic interactions between Cs and I. In contrast, both Cs_2CO_3 and $CsHCO_3$ show clear overlap between Cs 5p and O 2p orbitals, with a significant dispersion of the Cs 5p DOS with a width of more than 2.5 eV, indicating partial covalent bonding between Cs and O. This is further supported by Bader charge analysis, differential charge density and ELF in Fig.3c: in CsI, the Cs Bader charge approaches its formal ionic value, indicating nearly complete charge separation. In $CsHCO_3$ the Cs positive charge is slightly reduced and even more so in Cs_2CO_3, evidencing partial electron density redistribution toward Cs. Carbonate and bicarbonate phases display directional electron depletion near O and accumulation along the Cs–O axis and partially toward Cs, forming a polarized bridge region; CsI lacks any continuous accumulation between Cs and I, retaining spherical, isolated ionic basins. For ELF slices, along Cs–I, the inter-nuclear gap maintains a uniformly low ELF baseline (<0.30) with no mid-segment basin. In Cs_2CO_3 and $CsHCO_3$, after excluding near-nuclear regions, an extended intermediate ELF plateau (~0.30–0.35) develops along the Cs–O corridor; the corridor area fraction with ELF > 0.30 is markedly larger ($Cs_2CO_3 \approx 0.460$; $CsHCO_3 \approx 0.419$; CsI $\approx$ 0.000; Fig. 3d, Supplementary Discussion 3, Supplementary Table 1). This plateau is well below the high ELF values ($\approx$ 0.7–0.9) characteristic of strong covalent bonds, but it reveals directional polarization and weak p–p co-localization—a polarized partial-covalent character unique to Cs–O in these lattices. Taken together, the significant Cs 5p–O 2p DOS overlap and dispersion, the dipolar ΔQ redistribution, the reduced (less ionic) Bader charge on Cs, and the intermediate ELF plateau collectively rationalize the presence of the M-edge satellite tail in Cs_2CO_3 and $CsHCO_3$, while the absence of all four signatures in CsI explains the lack of a comparable tail.

The difference in tail intensity between $CsHCO_3$ and Cs_2CO_3 in the M-edge spectra correlates with the aggregate degree of polarized Cs–O bonding rather than a large increase in per-bond covalency. Bader charge analysis reveals that Cs ions in Cs_2CO_3 exhibit a slightly lower charge (+0.84 and +0.88) than the Cs ion in $CsHCO_3$ (+0.90), indicating more pronounced charge redistribution (partial electron back-polarization) for Cs_2CO_3. Atomic bond population analysis with the Crystal Orbital Hamiltonian Population (ICOHP) metrics further support this view: although the average per-bond ICOHP for "strong" Cs–O contacts (2.8–3.4 Å subset) is similar in the two phases (-0.170 vs -0.177 eV per bond, a negative ICOHP indicating a bonding interaction), Cs_2CO_3 hosts a substantially larger number of such interactions (26 vs 16) in the unit cell, yielding a more negative cumulative ICOHP (–4.41 vs –2.83 eV). When all identified Cs–O contacts are included, the total ICOHP in Cs_2CO_3 (–5.54 eV over 60 bonds) also exceeds that in $CsHCO_3$ (–3.28 eV over 28 bonds), reflecting a denser network of weak-to-moderate polarized bonds. Consistent with this, the Cs–O distance distribution for Cs_2CO_3 is shifted toward shorter separations (Supplementary Fig. 14b, d), increasing orbital overlap pathways for final-state screening. Taken together, these results indicate that the more extensive network of polarized partial-covalent Cs–O contacts in Cs_2CO_3—rather than a dramatic strengthening of any single bond—underpins its stronger M-edge satellite tail. Collectively, our experimental and computational results demonstrate that the intensity of satellite features in Cs M-edge spectra can serve as a sensitive probe of the strength and nature of interactions between Cs and its surrounding atoms.

To establish a baseline for interpreting *in situ* Cs M-edge spectra under electrochemical conditions—where cations are present in a solvated state—we further investigated the spectral evolution of Cs M-edges during the dissolution process. As shown in Fig. 3d, Cs_2CO_3 initially dried under vacuum calcination exhibits sharp satellite features at the previously identified energies, reflecting strong and well-defined Cs–O interactions in the crystalline lattice. However, upon gradual introduction of water vapor, these satellite features progressively broaden and eventually disappear at a water pressure of approximately 500 mTorr. The presence of water is expected to expand and/or distort the crystal lattice, leading to partial solvation. Once Cs^+ ions become fully solvated, a marked decrease in the tail intensity of the M-edge spectra is observed, indicating significantly weakened interactions between Cs^+ and its surrounding oxygen atoms. This weakening is consistent with the longer Cs–O distances in solvation shells compared to the short, directional Cs–O bonds in solid-state salts (Supplementary Fig.14). These results confirm that M-edge satellite intensity is sensitive not only to the chemical identity of neighboring atoms, but also to the local solvation structure, providing a valuable reference point for interpreting *in situ* measurements under electrochemical conditions.

The Cs-O interaction in the NOLI pocket

Building on our understanding of Cs M-edge spectral features, we next investigated the interaction between Cs^+ and various interfacial species within the Ag NOLI pocket using *in situ* Cs M-edge XAS. As outlined in Fig. 4a, Cs M-edge spectra were first collected at OCV, followed by catalyst preconditioning at –0.2 V_{RHE}. After preconditioning, the potential was returned to OCV, and Cs M-edge spectra were recorded every 20 minutes to monitor temporal changes.

It is important to note that directly measuring Cs M-edge TEY signals under –0.2 V_{RHE} is challenging. The large Faradaic current—typically on the order of microamperes in our setup—overwhelms the TEY signal, which is typically in the nanoampere range. Therefore, while the post-bias spectra may not perfectly capture the –0.2 V_{RHE} condition, their time-resolved evolution still offers valuable insights into interfacial Cs^+ behavior during catalysis. This is especially informative in the NOLI system, where the floating ligand layer restricts the rapid relaxation of the electric double layer once the bias is removed.

Before preconditioning, when the surfaces of Ag nanoparticles are chemisorbed with TDPA ligands, the Cs M-edge signal is weak in TEY mode, as shown in Fig. 4b. This is because Cs^+ ions reside outside the ligand layer at this stage, and the electrons emitted from these ions cannot reach the electrode due to the short mean free path. After applying -0.2 V_{RHE}, an overall enhancement in the TEY signal is observed, indicating increased local Cs^+ concentration at the electrode interface (Supplementary Fig.3). Concurrent O K-edge and SEIRAS measurements confirm reduced interfacial water content under bias, implying that Cs^+ ions at the interface are partially desolvated. Interestingly, at 0 minutes (i.e., immediately after returning to OCV), sharp satellite features emerge around 743 eV between the M_4 and M_5 edges, along with a broader tail feature centered at 757 eV. After 20 minutes, the 735–743 eV region becomes flattened, and the 757 eV feature diminishes significantly, continuing to fade by 40 minutes. Notably, these spectral changes are observed in TEY mode but absent in the bulk-sensitive TFY mode (Fig. 4c), confirming that the spectral variations arise from the interfacial region rather than the bulk electrolyte.

The strong satellite features at 0 minutes reflect a pronounced interaction between Cs^+ and oxygen-containing species during catalysis. Within the NOLI pocket, several species could contribute to this interaction. First, Cs^+ may coordinate with the phosphonic acid groups of TDPA ligands, as supported by O K-edge data. Indeed, Cs–TDPA complexes display pronounced satellite features in their M-edge spectra (Supplementary Fig.15). Second, although Cs–H_2O interactions typically do not give rise to sharp satellite features, our prior work on graphene–electrolyte interfaces shows that at extremely high interfacial Cs^+ concentrations (~8 M), satellite features can emerge[54]. At such high local concentrations, even without applying bias, Cs^+ becomes partially desolvated and forms Cs-anion pairs. At the same time, the high concentration forces water molecules to approach closer to the Cs to compensate for the accumulated positive charge. The Cs-anion interaction and/or strengthened Cs–H_2O interactions can generate a noticeable satellite feature detectable by XAS[54]. Finally, given the applied bias and CO_2-saturated environment, the observed features could originate from direct interactions between desolvated Cs^+ and surface adsorbates, e.g. surface hydroxyl (*OH), which has been recently reported[35], or reaction intermediates, particularly $*CO_2^-$, as supported by SEIRAS data.

To further elucidate the origin of the satellite features, we conducted *in situ* Cs M-edge measurements during an online electrolyte exchange from CO_2- to Ar-saturated conditions at OCV. During the exchange, we observed a gradual decline in the intensity of the M_4 and M_5 main edges (Supplementary Fig.16), indicating a decrease in interfacial Cs^+ concentration. This result is corroborated by electrochemical capacitance measurements showing lower ion concentration under Ar versus CO_2 saturated conditions (Supplementary Fig.17). After the Cs signal stabilized, the

same measurement protocol was repeated: preconditioning at –0.2 V_{RHE} followed by spectral acquisition every 17 minutes. Under Ar, the Cs M-edge intensity did not recover to the level observed under CO_2, confirming that CO_2 is required to maintain a high interfacial Cs^+ concentration. As shown in Fig. 4d and Supplementary Fig.18, while a weak 757 eV satellite feature appeared at 0 minutes, its intensity was markedly lower than that under CO_2-saturated conditions. Upon reintroduction of CO_2, the satellite feature promptly recovered (Supplementary Fig.19). Since Cs–ligand, Cs–HCO_3^-/Cs-CO_3^{2-}, and Cs–H_2O interactions remain largely unchanged between Ar and CO_2 conditions, these observations point to interactions with CO_2-derived surface intermediates as the origin of the satellite features. Alternative assignments—for instance, Cs–*OH interactions—can be ruled out, since under Ar conditions the coverage of *OH (if present) should be higher due to the absence of competitive adsorption of CO_2 intermediates, and would thus be expected to produce a stronger, not weaker, satellite signal. Instead, the observed trend is fully consistent with a direct interaction between desolvated Cs^+ and CO_2-derived intermediates, most likely adsorbed $*CO_2^-$. DFT calculations further support this conclusion. The DOS of adsorbed $*CO_2^-$ stabilized by a partially desolvated Cs^+ (Fig. 4e) shows significant orbital overlap between Cs 5p and O 2p states in the –6 to –12 eV region, as well as additional Cs 5s–O 2s overlap below –20 eV. S orbital overlapping is negligible in salt crystals like $CsHCO_3$ and Cs_2CO_3, suggesting an even stronger Cs–O interaction in the adsorbed $*CO_2^- \cdots Cs^+$ complex.

To mechanistically rationalize how desolvated Cs^+ promotes CO_2 activation, we generated seven idealized interfacial states (Fig. 4f) that discretize a "desolvation coordinate" from Cs^+ with 6 explicit H_2O molecules, $Cs^+(6H_2O)$ (outer Helmholtz / diffuse layer–like environment)[54,55] to $Cs^+(1H_2O)$ (extreme near-surface coordination). These states are thermodynamic sampling points rather than a presumed kinetic pathway. We employed grand canonical DFT (GC-DFT) calculations and evaluated a grand free energy of CO_2 adsorption ($\Delta\Omega$) referenced to the clean Ag (111) surface with a solvated Cs^+, and the Gibbs free energy of solvated CO_2. Details can be found in Materials and Methods. We used hydrated $Cs^+(6H_2O)$ far from the interface as the reference point, where a physiosorbed, nearly linear CO_2 (O–C–O = 179.9°, average Cs–O = 4.56 Å) is observed. Slight disruption (lower symmetry) of the solvation shell ($6H_2O$) begins to bend the CO_2 (angle → 171.0°) at the Ag surface (Fig. 4g). Progressive water removal (5→$1H_2O$) shortens Cs–O (of CO_2) from 3.51 → 2.83 Å and CO_2–Ag contact from 2.82 → 2.19 Å, while ICOHP(Cs–O) magnitudes become more negative (–0.11, –0.14, –0.18, –0.19, -0.20 eV for 5, 4, 3, 2, $1H_2O$ respectively; Fig. 4h), evidencing an increasing partial covalent component in Cs-O bond. This enhanced interaction yields a more "activated" $*CO_2$ intermediate that is structurally predisposed for downstream protonation (Fig. 1f).

Potential-dependent $\Delta\Omega$ profiles (Fig. 4i) show several crossovers: Above -0.1 V_{RHE}, $Cs^+(3H_2O)$ minimizes $\Delta\Omega$; between -0.1 V_{RHE} to –0.8 V_{RHE} a ($2H_2O$) state becomes competitive, and more negative than –0.8 V_{RHE} the ($1H_2O$) state is lowest. These results suggest that under increasingly reductive conditions, activated CO_2 is preferentially stabilized by Cs^+ with progressively higher degrees of desolvation. Since such desolvated cation–intermediate interactions are thermodynamically promoted by applied bias, we propose that they are not unique to ligand-defined NOLI interfaces but represents a general feature of electrochemical solid–liquid interfaces once cation desolvation can be sustained.

In conventional ligand-free metal electrodes operated in dilute aqueous electrolytes, cations are expected to remain largely solvated, limiting the magnitude and persistence of such specific interactions. This provides a natural explanation for why cation effects are commonly observed on bare metal surfaces yet are typically more modest and highly sensitive to electrolyte identity and operating conditions. In contrast, the NOLI architecture stabilizes a locally ion-rich, water-deficient interfacial microenvironment, thereby amplifying the population of desolvated Cs^+ ions and rendering their direct interaction with $*CO_2^-$ experimentally observable and catalytically significant.

More broadly, similar desolvation-enabled cation–intermediate interactions may be accessible in other confined or low-water-activity interfacial environments, such as highly concentrated electrolytes[34], ionic-liquid–containing media[56], and nanoporous or ionomer-containing electrodes[57,58], where ion crowding and restricted solvation are more likely to occur. Altogether, these insights underscore the importance of interfacial design—specifically, engineering ion-rich, water-deficient microenvironments—as a general strategy to harness desolvated cation–intermediate interactions for enhancing reactivity across a wide range of electrochemical transformations.

Conclusion

In this study, we combined *in situ* vibrational, X-ray spectroscopic techniques and first principles simulations to elucidate the solvation structure and interfacial behavior of Cs^+ under CO_2-reducing conditions. SEIRAS measurements captured the full evolution of the Cs^+ solvation environment under applied bias, revealing that within the catalyst–electrolyte interface confined by a detached ligand layer, desolvated cations facilitate CO_2 activation at unusually low overpotentials. This phenomenon directly accounts for the enhanced CO_2 reduction activity observed in this NOLI system. *In situ* XAS measurements further revealed that the promotional effect of desolvated cations originates from direct interactions between Cs^+ and surface-bound intermediates. Notably, DFT-assisted XAS analysis showed that the interaction between desolvated Cs^+ and $*CO_2^-$ species possesses partial covalent character, demonstrating that cations can stabilize intermediates, and thus modulate electrochemical reactions through mechanisms beyond purely electrostatic stabilization.

Altogether, this work provides direct spectroscopic evidence of desolvated Cs^+ under *operando* conditions and clarifies its role in stabilizing $*CO_2^-$ intermediates, enabling efficient CO_2-to-CO conversion at low overpotentials. Moreover, we highlight that desolvated cations can engage in orbital hybridization with key intermediates, thereby influencing reaction kinetics through direct electronic effects. Our findings highlight that ligand-realized, ion-rich interfacial confinement is a powerful and generalizable design principle for catalytic systems seeking to harness and amplify cation effects. This strategy opens new avenues for microenvironment engineering to optimize activity and selectivity across a wide range of electrochemical reactions.

Methods

Synthesis of Ag Nanoparticles

Silver nanoparticles (Ag NPs) were synthesized following previously reported procedures[18]. In a three-neck flask, 10 mL of trioctylamine (Sigma-Aldrich, 98%) was degassed with nitrogen at 130 °C for 30 minutes. After cooling to room temperature, 0.50 mmol of silver(I) acetate (Sigma-Aldrich, 99.99%) and 0.25 mmol of tetradecylphosphonic acid (TDPA, Sigma-Aldrich, 98%) were added. The mixture was heated at 130 °C for 1 hour under a nitrogen atmosphere. Upon cooling to 50 °C, the reaction mixture was transferred to a centrifuge tube, and 35 mL of ethanol was added to precipitate the nanoparticles. After centrifugation at 6,000 rpm for 15 minutes, the nanoparticles were redispersed in 10 mL of hexane. To further narrow the particle size distribution, acetone (~10 mL) was added dropwise to induce turbidity, followed by centrifugation at 12,000 rpm for 10 minutes. The final nanoparticles were redispersed in hexane for storage.

Preparation of Cs–TDPA complex

TDPA was dissolved in ethanol to a final concentration of 50 mM. CsOH powder was gradually added to the solution until the Cs^+ concentration reached 0.1 M. Dissolved TDPA and CsOH are expected to undergo an acid-base reaction, forming the Cs-TDPA compound, where oxygen atoms of TDPA directly interact with Cs cation.

Electrochemical Measurements

All electrochemical measurements were performed in a custom-built H-cell. The Ag/AgCl (3 M KCl, World Precision Instruments) electrode was used as the reference, and a platinum wire served as the counter electrode. The potentiostat (Biologic) automatically compensated for 85% of the solution resistance; the remaining 15% was manually corrected in post-processing. For catalyst preparation, 29 μg of Ag NPs were drop-cast onto a 1 cm^2 carbon paper electrode (Toray 29AA).

Gaseous reaction products were analyzed using a gas chromatograph (SRI Instruments) equipped with both thermal conductivity (TCD) and flame ionization (FID) detectors. Product-specific Faradaic efficiencies (FEs) were determined by converting the quantified molar production rates into charge equivalents and normalizing to the total charge passed during electrolysis. To reliably quantify the FE values at low current densities, the surface area of the working electrode was increased, and the CO_2 flow rate was reduced to 5 sccm when total current is below 0.5 mA (compared to 20 sccm used at higher current densities), allowing gas products to accumulate to higher concentrations prior to gas chromatograph analysis and ensures that detected signals remain well above the instrument's quantification limit.

The ECSA of the Ag–NOLI catalysts was quantified using the Pb underpotential deposition (UPD) method, following a procedure that was reported previously[18]. Briefly, cyclic voltammetry was performed between −0.10 and −0.45 V vs. Ag/AgCl (1 M KCl) at a scan rate of 50 mV s^{-1} in an electrolyte containing 3 mM $Pb(ClO_4)_2$, 10 mM $HClO_4$, and 100 mM $NaClO_4$. A polished Ag foil with a geometric area of 2 cm^2 was used as the reference, and its Pb stripping charge (361.7 μC cm^{-2}) was taken as the standard for calculating the ECSA of the Ag–NOLI catalysts.

Electrochemical impedance spectroscopy (EIS) measurements were performed to quantify the electrochemical double-layer capacitance of the Ag–NOLI electrode. All EIS experiments were conducted in 0.1 M $CsHCO_3$ electrolyte. Impedance spectra were collected by applying a 10 mV AC perturbation over a frequency range from 100 kHz to 100 mHz, with eight data points per decade. Each measurement was repeated three times to ensure reproducibility. The resulting spectra were analyzed using an equivalent circuit consisting of a solution resistance (R_s) in series with a parallel combination of a constant phase element (CPE, Q) and charge-transfer resistance (R_{ct}). CPE was used in place of an ideal capacitor to account for non-ideal capacitive behavior of the electrochemical double layer[59]. The fitted CPE exponent (α) was greater than 0.9 across all measurements, indicating near-ideal capacitive response. Accordingly, the Q values were taken as close approximations of the double-layer capacitance (C_{dl}).

Electrode Preparation for SEIRAS

The reflecting surface of a 60° Si prism (Pike Technologies) was polished sequentially with 6 μm, 1 μm, and 0.25 μm diamond pastes for 10 minutes each to expose a fresh Si surface. The prism was then rinsed with deionized (DI) water and sonicated in DI water, acetone, and DI water for 10 minutes each. After cleaning, the prism surface was etched in 5 mL of 40 wt% NH_4F solution at 25 °C for 2 minutes to achieve a hydrogen-terminated surface, followed by thorough rinsing with DI water.

Gold films were deposited by immersing the etched Si prism in a gold plating solution at 60 °C for 200 seconds. The plating solution was prepared by adding 200 μL of 49% HF to a 10 mL aqueous mixture containing 10 mM $NaAuCl_4{\cdot}2H_2O$, 100 mM Na_2SO_3, 33 mM $Na_2S_2O_3{\cdot}5H_2O$, and 33 mM NH_4Cl. To improve film adhesion and uniformity, the freshly deposited gold layer was first removed using aqua regia, followed by re-plating until a smooth, mirror-like surface was obtained. A high-quality gold film exhibited a resistance less than 10 Ω.

Before catalyst deposition, the Au film was electrochemically activated by cycling the potential between 0.2 V and 1.5 V (vs. 3M Ag/AgCl) in 0.1 M H_2SO_4 for three cycles. This step is critical for cleaning the surface and enable enough surface enhancement effects. The activated Au films were rinsed with DI water and dried under nitrogen. For Ag NP measurements, 35 μg of Ag NPs were drop-cast onto the Au-coated prism. For Ag film controls samples, a 50 nm Ag film was deposited directly onto the activated Au surface by thermal evaporation.

***In Situ* SEIRAS Measurements**

The catalyst-loaded Si prism was assembled into a custom electrochemical cell and mounted onto a VeeMax III ATR accessory (Pike Technologies). Infrared spectra were collected using a nitrogen-purged Bruker Vertex 70 FTIR spectrometer equipped with a mercury cadmium telluride (MCT) detector. Spectra were recorded with a 4 cm^{-1} resolution, 32-scan averaging, and a scan velocity of 20 kHz during linear sweep voltammetry (2 mV/s). Each spectrum acquisition took approximately 50 seconds, and the reported potential corresponds to the end of the acquisition period. All SEIRAS spectra are reported as absorbance, calculated using:

$$Abs. = -\log_{10}\frac{S}{R}$$

where S is the single-beam sample spectrum and R is the single-beam reference spectrum.

STEM measurement

EC-STEM and 4D-STEM were collected on the FEI ThemIS instrument at the molecular foundry, LBNL. The liquid cell setup consisted of a Protochips Poseidon AX holder and two silicon chips with silicon nitride windows sandwiching a 500 nm electrolyte layer. The bottom chip features a three-electrode setup with glassy carbon working electrode, Pt counter electrode, and Pt pseudo-reference electrode. Ag NOLI was dropcast onto the glassy carbon working electrode. The beam current was set to < 1 pA to avoid beam damage, and the convergence angle was 0.46 mrad. 4D-STEM was collected on a Gatan K2 camera in *in situ* mode. Data was processed using the py4DSTEM python library[60].

XAS measurement

In situ XAS experiments were conducted at three synchrotron facilities: beamline 8.0.1.4 and 9.0.1 of the Advanced Light Source (ALS), Lawrence Berkeley National Laboratory (USA), and beamline B07 at the Diamond Light Source (UK). At ALS, the measurements were performed using a custom-built liquid flow cell featuring an ultrathin Si_3N_4 membrane (100 nm thickness), which serves as the X-ray transparent window and separates the liquid-phase electrochemical environment from the ultrahigh vacuum of the beamline. To ensure conductivity, the membrane was coated with 10 nm of Pt. The electrochemical setup inside the cell included a calibrated Ag/AgCl (3 M KCl) reference electrode and a platinum wire as the counter electrode.

At the Diamond Light Source, an in-house electrochemical flow cell[61] was employed. This setup included a platinum wire counter electrode and an Ag/AgCl-coated silver wire as the reference electrode. The continuous Si_3N_4 window (100 nm thickness) was coated with 2.5 nm of Cr as adhesive layer, a 10 nm layer of gold as current collector, followed by three layers of graphene. The quality and coverage of the graphene layer were verified by scanning electron microscopy (SEM) and Raman spectroscopy to ensure minimal defects and uniform coverage.

For *in situ* measurements, the Ag NOLI sample was prepared by drop-casting Ag nanoparticles onto the Si_3N_4 membrane at a loading of 50 $\mu g\ cm^{-2}$. For Ag film control samples, a 2.5 nm chromium adhesion layer followed by a 15 nm silver film was deposited onto the Si_3N_4 window by thermal evaporation.

The XAS spectra of reference salts were measured on Beamline 9.3.2 of the ALS and B07 of the Diamond Light Source. Samples on 9.3.2 were dropcast and measured on a polished gold foil, all samples were dropcast as 3 ul droplets from a saturated solution and dried in a nitrogen box. A platinum heater sample holder was used for temperature control and purified water for humidity control. The XPS capabilities of 9.3.2 were used to find a thin layer of salt at the outer edges of the coffee ring, to reduce charging and solid-state effects. Gold was used as a current collector for the drain current measurements. Therefore, the thermocouple was connected to a SR560 preamplifier. To verify that the observed Cs-Oxygen interactions are not an effect of Cs-electrode interaction, or background drift from the drain current measurement, the XPS analyzer was employed to simultaneously measure the secondary electron yield, by collecting low energy electrons with a kinetic energy of 40 eV. Reference measurements at the Diamond light source were performed on a p-doped SI wafer. Dropcasting was performed in a similar manner than the 9.3.2 samples. Fluorescent

yield and drain current measurements were employed at the same time to verify that the observed spectral features are not an effect of electron based XAS detection methods.

Density Functional Theory details

All periodic density-functional theory (DFT) calculations were performed with the Vienna Ab initio Simulation Package (VASP)[62]sing the projector-augmented wave (PAW) method[63] and the PBE exchange–correlation functional within the generalized gradient approximation (GGA), augmented by the dDsC dispersion correction to include van der Waals interactions[64,65]. A plane-wave kinetic-energy cutoff of 400 eV was used in all stages (converged to < ~1 meV per atom in test calculations). Gas-phase and bulk structural relaxations were first carried out in vacuum until the maximum residual force fell below 0.01 eV $Å^{-1}$ and the total energy change was $< 10^{-6}$ eV. Subsequent implicit-solvation optimizations employed VASPsol[66,67] with force and energy convergence criteria of 0.02 eV $Å^{-1}$ and 10^{-6} eV, respectively.

For bulk crystals (Cs_2CO_3, $CsHCO_3$, CsI) the Brillouin zone was sampled with a Γ-centered 5 × 5 × 5 Monkhorst–Pack grid during geometry optimization. Surface models used a three-layer Ag (111) (4 × 4) supercell (bottom layer fixed), a 15 Å vacuum gap along z, and a 5 × 5 × 1 k-point grid for relaxation. For implicit-solvation and grand-canonical DFT (GC-DFT) treatments, the simulation cell height was extended to 60 Å to host the dielectric continuum while retaining the atomically explicit slab and adsorbates; slab symmetry operations were preserved where applicable.

High-accuracy single-point calculations for projected density of states (pDOS), Bader charge analysis, differential charge density (Δϱ), electron localization function (ELF), and bonding (COHP) metrics used denser Γ-centered meshes of 8 × 8 × 8 (bulk) and 8 × 8 × 1 (slabs). COHP and integrated –ICOHP values were obtained with LOBSTER (pbeVaspFit2015 basis)[68] after verifying a charge spilling < 2 %. Bader charges were computed on the all-electron charge density reconstructed from the PAW potentials with a fine FFT grid (spacing ⩽ ~0.10 Å). Differential charge densities were generated as ϱ_total – Σϱ_frag (identical supercells, fragment geometries frozen to the combined state). ELF was evaluated on the self-consistent real-space grid and analyzed via selected z slices and line profiles along Cs–O (or Cs–intermediate) axes.

Grand-Canonical DFT calculations

The grand canonical free energy was evaluated by grand canonical density functional theory (GCDFT) calculations, which is a surface charging technique. Details can be found in our previous work, and here we summarize the key points[69,70] The net charge of the surface *n*surface is obtained as:

$$n_{surface} = N_{surface} - N_{surface,neutral}$$

Where $N_{surface}$ and $N_{surface,neutral}$ is the number of electrons on the surface and the number of electrons in the neutral state. DFT energy for the charged surface is obtained as:

$$E_{surface} = E_{surface,raw} + \epsilon_{fermishift} n_{surface}$$

Where $E_{surface,raw}$ is the raw electronic energy of the surface and $\epsilon_{fermishift} n_{surface}$ is the correction term accounting for the difference ($\epsilon_{fermishift}$) in the reference energy of the electron between the "internal" reference level and vacuum. Then, the grand canonical electronic energy of a surface model, $\Omega(U)$ is obtained as:

$$\Omega(U) = E_{surface} - n_{surface}\mu_{electron}$$

Where $\mu_{electron}$ is the chemical potential of an electron, which is defined as:

$$\mu_{electron} = qU_{vac} = -eU_{vac}$$

Where U_{vac} is the potential of the system with reference to the vacuum level and q is the charge of an electron. The potential of the system with reference to the vacuum can be determined by two components, the Fermi level (ϵ_F) with reference to the "internal" zero energy reference and the Fermi shift which is the difference between the "internal" energy reference and the vacuum level:

$$-eU_{vac} = \epsilon_F + \epsilon_{fermishift}$$

For the metallic systems, the potential-dependent grand canonical energy, $\Omega(U)$, exhibits a quadratic behaviour around the potential of zero charge ($U0$) in the vacuum scale:

$$\Omega(U) = \Omega(U_0) - \frac{1}{2}C(U - U_0)^2$$

Where C is the capacitance of the surface. The potential of the system with respect to the standard hydrogen electrode (SHE) can be converted from U_{vac} as:

$$U_{SHE} = U_{vac} - 4.44$$

The linearized Poisson Boltzmann implicit solvation model implemented in VASPsol[67] is used to represent the polarizable electrolyte region. The dielectric constant of water, 78.4, and the Debye screening length corresponding to 0.1 M concentration of electrolytes, 9.6 Å, were used. The surface slab is symmetrized along the z-axis to avoid asymmetric potential in the implicit solvation region. Here the implicit solvent thickness is set to 60 Å for the symmetrized slab.

Grand Canonical Free Energy Calculations of CO_2 Adsorption

To evaluate the thermodynamic stability of *CO_2 adsorption configurations with different degrees of Cs^+ desolvation under applied potential, we employed grand-canonical DFT (GC-DFT). For each configuration containing adsorbed *CO_2, an interfacial Cs^+ cation, and n explicitly modeled water molecules on Ag (111), we define the grand free energy of CO_2 adsorption at electrode potential U (vs. RHE) as

$$\Delta\Omega(U) = G(U)_{Ag111\cdot CO_2\cdot Cs^{+1}\cdot(H_2O)n} - G(U)_{Ag111\cdot Cs^{+1}\cdot(H_2O)_n} - G_{CO_2} \qquad \text{Eq. 1}$$

where $G(U)_{Ag111\cdot CO_2\cdot Cs^{+1}\cdot(H_2O)n}$ is the Gibbs free energy at electrode potential U of the Ag(111) slab bearing an adsorbed *CO_2, an interfacial Cs^+, and n explicit water molecules, which is referenced to a clean Ag (111) surface with an adsorbed

solvated Cs^+ with n explicit water molecules, $G(U)_{Ag111\cdot Cs^{+1}\cdot(H_2O)_n}$, and the free energy of solution-phase *CO_2, G_{CO_2}(approximated as gas-phase *CO_2 with one-half of its gas-phase entropy to mimic dissolution).

Data availability

Data supporting the findings of this study are available upon reasonable request from the corresponding authors.

Reference

1 De Luna, P. *et al.* What would it take for renewably powered electrosynthesis to displace petrochemical processes. *Science* **364**, eaav3506 (2019).
2 Nitopi, S. *et al.* Progress and Perspectives of Electrochemical CO_2 Reduction on Copper in Aqueous Electrolyte. *Chemical Reviews* **119**, 7610-7672 (2019).
3 Thorson, M. R., Siil, K. I. & Kenis, P. J. A. Effect of Cations on the Electrochemical Conversion of CO_2 to CO. *Journal of The Electrochemical Society* **160**, F69 (2013).
4 Yu, S. *et al.* CO_2-to-methanol electroconversion on a molecular cobalt catalyst facilitated by acidic cations. *Nature Catalysis* **7**, 1000-1009 (2024).
5 Monteiro, M. C. O. *et al.* Absence of CO_2 electroreduction on copper, gold and silver electrodes without metal cations in solution. *Nature Catalysis* **4**, 654-662 (2021).
6 Zhang, Z.-M. *et al.* Probing electrolyte effects on cation-enhanced CO_2 reduction on copper in acidic media. *Nature Catalysis* **7**, 807-817 (2024).
7 Gunathunge, C. M., Ovalle, V. J. & Waegele, M. M. Probing promoting effects of alkali cations on the reduction of CO at the aqueous electrolyte/copper interface. *Physical Chemistry Chemical Physics* **19**, 30166-30172 (2017).
8 Murata, A. & Hori, Y. Product Selectivity Affected by Cationic Species in Electrochemical Reduction of CO_2 and CO at a Cu Electrode. *Bulletin of the Chemical Society of Japan* **64**, 123-127 (1991).
9 Singh, M. R., Kwon, Y., Lum, Y., Ager, J. W., III & Bell, A. T. Hydrolysis of Electrolyte Cations Enhances the Electrochemical Reduction of CO_2 over Ag and Cu. *Journal of the American Chemical Society* **138**, 13006-13012 (2016).
10 Cui, Z., Wong, A. J.-W., Janik, M. J. & Co, A. C. Cation effects on CO_2 reduction catalyzed by single-crystal and polycrystalline gold under well-defined mass transport conditions. *Science Advances* **11**, eadr6465 (2025).
11 Chen, L. D., Urushihara, M., Chan, K. & Nørskov, J. K. Electric Field Effects in Electrochemical CO_2 Reduction. *ACS Catalysis* **6**, 7133-7139 (2016).
12 Gu, J. *et al.* Modulating electric field distribution by alkali cations for CO_2 electroreduction in strongly acidic medium. *Nature Catalysis* **5**, 268-276 (2022).
13 Ayemoba, O. & Cuesta, A. Spectroscopic Evidence of Size-Dependent Buffering of Interfacial pH by Cation Hydrolysis during CO_2 Electroreduction. *ACS Applied Materials & Interfaces* **9**, 27377-27382 (2017).
14 Koper, M. T. M. Theory and kinetic modeling of electrochemical cation-coupled electron transfer reactions. *Journal of Solid State Electrochemistry* **28**, 1601-1606 (2024).
15 Qin, X., Hansen, H. A., Honkala, K. & Melander, M. M. Cation-induced changes in the inner- and outer-sphere mechanisms of electrocatalytic CO2 reduction. *Nature Communications* **14**, 7607 (2023).
16 Shin, S.-J. *et al.* A unifying mechanism for cation effect modulating C_1 and C_2 productions from CO_2 electroreduction. *Nature Communications* **13**, 5482 (2022).
17 Zhang, Z. *et al.* Molecular understanding of the critical role of alkali metal cations in initiating CO2 electroreduction on Cu(100) surface. *Nature Communications* **15**, 612 (2024).
18 Kim, D. *et al.* Selective CO_2 electrocatalysis at the pseudocapacitive nanoparticle/ordered-ligand interlayer. *Nature Energy* **5**, 1032-1042 (2020).
19 Kim, D., Kley, C. S., Li, Y. & Yang, P. Copper nanoparticle ensembles for selective electroreduction of CO_2 to C_2-C_3 products. *Proceedings of the National Academy of Sciences* **114**, 10560-10565 (2017).
20 Shan, Y. *et al.* Nanometre-resolved observation of electrochemical microenvironment formation at the nanoparticle–ligand interface. *Nature Catalysis* **7**, 422-431 (2024).
21 Yang, Y. *et al.* Operando studies reveal active Cu nanograins for CO_2 electroreduction. *Nature* **614**, 262-269 (2023).
22 Corson, E. R. *et al.* In Situ ATR–SEIRAS of Carbon Dioxide Reduction at a Plasmonic Silver Cathode. *Journal of the American Chemical Society* **142**, 11750-11762 (2020).
23 Oda, I., Ogasawara, H. & Ito, M. Carbon Monoxide Adsorption on Copper and Silver Electrodes during Carbon Dioxide Electroreduction Studied by Infrared Reflection Absorption Spectroscopy and Surface-Enhanced Raman Spectroscopy. *Langmuir* **12**, 1094-1097 (1996).

24 Ye, K. *et al.* Molecular level insights on the pulsed electrochemical CO_2 reduction. *Nature Communications* **15**, 9781 (2024).
25 Firet, N. J. & Smith, W. A. Probing the Reaction Mechanism of CO_2 Electroreduction over Ag Films via Operando Infrared Spectroscopy. *ACS Catalysis* **7**, 606-612 (2017).
26 Müslehiddinoğlu, J. & Vannice, M. A. CO adsorption on supported and promoted Ag epoxidation catalysts. *Journal of Catalysis* **213**, 305-320 (2003).
27 Ertl, G., Neumann, M. & Streit, K. M. Chemisorption of CO on the Pt(111) surface. *Surface Science* **64**, 393-410 (1977).
28 Gunasooriya, G. T. K. K. & Saeys, M. CO Adsorption on Pt(111): From Isolated Molecules to Ordered High-Coverage Structures. *ACS Catalysis* **8**, 10225-10233 (2018).
29 Steininger, H., Lehwald, S. & Ibach, H. On the adsorption of CO on Pt(111). *Surface Science* **123**, 264-282 (1982).
30 Cui, Z., Wong, A. J.-W., Janik, M. J. & Co, A. C. Negative Reaction Order for CO during CO2 Electroreduction on Au. *Journal of the American Chemical Society* **146**, 23872-23880 (2024).
31 Moradzaman, M. & Mul, G. Infrared Analysis of Interfacial Phenomena during Electrochemical Reduction of CO_2 over Polycrystalline Copper Electrodes. *ACS Catalysis* **10**, 8049-8057 (2020).
32 Miki, A., Ye, S. & Osawa, M. Surface-enhanced IR absorption on platinum nanoparticles: an application to real-time monitoring of electrocatalytic reactions. *Chemical Communications*, 1500-1501 (2002).
33 Zhu, S., Jiang, B., Cai, W.-B. & Shao, M. Direct Observation on Reaction Intermediates and the Role of Bicarbonate Anions in CO_2 Electrochemical Reduction Reaction on Cu Surfaces. *Journal of the American Chemical Society* **139**, 15664-15667 (2017).
34 Zhang, H., Gao, J., Raciti, D. & Hall, A. S. Promoting Cu-catalysed CO_2 electroreduction to multicarbon products by tuning the activity of H_2O. *Nature Catalysis* **6**, 807-817 (2023).
35 Liu, Q. & Yang, W. Resolving non-covalent interactions between surface hydroxyl on Cu and interfacial water in alkaline CO electroreduction. *Nature Catalysis* **8**, 843-852 (2025).
36 Wang, Y.-H. *et al.* In situ Raman spectroscopy reveals the structure and dissociation of interfacial water. *Nature* **600**, 81-85 (2021).
37 Delmo, E. P. *et al.* In Situ Infrared Spectroscopic Evidence of Enhanced Electrochemical CO_2 Reduction and C–C Coupling on Oxide-Derived Copper. *Journal of the American Chemical Society* **146**, 1935-1945 (2024).
38 Diesen, E. *et al.* Rationalizing the "anomalous" electrochemical Stark shift of CO at Pt(111) through vibrational spectroscopy and density-functional theory calculations. *Surface Science* **754**, 122694 (2025).
39 Figueiredo, M. C., Hiltrop, D., Sundararaman, R., Schwarz, K. A. & Koper, M. T. M. Absence of diffuse double layer effect on the vibrational properties and oxidation of chemisorbed carbon monoxide on a Pt(111) electrode. *Electrochimica Acta* **281**, 127-132 (2018).
40 Timoshenko, J. & Roldan Cuenya, B. In Situ/Operando Electrocatalyst Characterization by X-ray Absorption Spectroscopy. *Chemical Reviews* **121**, 882-961 (2021).
41 Frazer, B. H., Gilbert, B., Sonderegger, B. R. & De Stasio, G. The probing depth of total electron yield in the sub-keV range: TEY-XAS and X-PEEM. *Surface Science* **537**, 161-167 (2003).
42 Velasco-Velez, J.-J. *et al.* The structure of interfacial water on gold electrodes studied by x-ray absorption spectroscopy. *Science* **346**, 831-834 (2014).
43 Frati, F., Hunault, M. O. J. Y. & de Groot, F. M. F. Oxygen K-edge X-ray Absorption Spectra. *Chemical Reviews* **120**, 4056-4110 (2020).
44 Nilsson, A. *et al.* X-ray absorption spectroscopy and X-ray Raman scattering of water and ice; an experimental view. *Journal of Electron Spectroscopy and Related Phenomena* **177**, 99-129 (2010).
45 Guo, J. & Luo, Y. Molecular structure in water and solutions studied by photon-in/photon-out soft X-ray spectroscopy. *Journal of Electron Spectroscopy and Related Phenomena* **177**, 181-191 (2010).
46 Smith, J. W. & Saykally, R. J. Soft X-ray Absorption Spectroscopy of Liquids and Solutions. *Chemical Reviews* **117**, 13909-13934 (2017).
47 Lange, K. M., Hodeck, K. F., Schade, U. & Aziz, E. F. Nature of the Hydrogen Bond of Water in Solvents of Different Polarities. *The Journal of Physical Chemistry B* **114**, 16997-17001 (2010).
48 Nordlund, D. *et al.* Sensitivity of x-ray absorption spectroscopy to hydrogen bond topology. *Physical Review B* **80**, 233404 (2009).
49 Messer, B. M. *et al.* pH Dependence of the Electronic Structure of Glycine. *The Journal of Physical Chemistry B* **109**, 5375-5382 (2005).
50 Wu, C. H. *et al.* Molecular-Scale Structure of Electrode–Electrolyte Interfaces: The Case of Platinum in Aqueous Sulfuric Acid. *Journal of the American Chemical Society* **140**, 16237-16244 (2018).
51 Ji, S. G. *et al.* Alkali metal cations act as homogeneous cocatalysts for the oxygen reduction reaction in aqueous electrolytes. *Nature Catalysis* **7**, 1330-1338 (2024).
52 Suzuki, C. *et al.* Evaluation of electronic state of Cs-adsorbed clay minerals by NEXAFS analysis using DFT calculations. *Journal of Physics and Chemistry of Solids* **127**, 169-177 (2019).
53 Minasian, S. G. *et al.* Quantitative Evidence for Lanthanide-Oxygen Orbital Mixing in CeO_2, PrO_2, and TbO_2. *Journal of the American Chemical Society* **139**, 18052-18064 (2017).
54 Falling L, J. M., Zhao X, Girotto G, Altoe V, van Spronsen M, et al. The Anomalous Behavior of Cesium in the Electrical Double Layer: an In-Situ X-ray Spectroscopy Study on Graphene. *ChemRxiv* (2024).
55 Marcus, Y. Effect of ions on the structure of water. *Pure and Applied Chemistry* **82**, 1889-1899 (2010).

56 Yang, D., Zhu, Q. & Han, B. Electroreduction of CO2 in Ionic Liquid-Based Electrolytes. *The Innovation* **1**, 100016 (2020).
57 Liu, Z. *et al.* Sustainable and Efficient Bicarbonate Electrolysis via Enhanced CO2 and Cation Availability on a Gas–Water Dual-Permeable Electrode. *Journal of the American Chemical Society* **148**, 2039-2047 (2026).
58 Ruan, S. *et al.* Ionomers modulate the microenvironment in electrocatalytic CO2 reduction. *Chemical Science* **17**, 96-117 (2026).
59 Lazanas, A. C. & Prodromidis, M. I. Electrochemical Impedance Spectroscopy—A Tutorial. *ACS Measurement Science Au* **3**, 162-193 (2023).
60 Savitzky, B. H. *et al.* py4DSTEM: A Software Package for Four-Dimensional Scanning Transmission Electron Microscopy Data Analysis. *Microscopy and Microanalysis* **27**, 712-743 (2021).
61 Grinter, D. C., Ferrer, Pilar, Venturini, Federica, van Spronsen, Matthijs A., Large, Alexander I., Kumar, Santosh, Jaugstetter, Maximilian, Iordachescu, Alex, Watts, Andrew, Schroeder, Sven L. M., Kroner, Anna, Grillo, Federico, Francis, Stephen M., Webb, Paul B., Hand, Matthew, Walters, Andrew, Hillman, Michael, Held, Georg, . VerSoX B07-B: a high-throughput XPS and ambient pressure NEXAFS beamline at Diamond Light Source. *Journal of Synchrotron Radiation* **31**, 578-589 (2024).
62 Kresse, G. & Furthmüller, J. Efficiency of ab-initio total energy calculations for metals and semiconductors using a plane-wave basis set. *Computational Materials Science* **6**, 15-50 (1996).
63 Kresse, G. & Joubert, D. From ultrasoft pseudopotentials to the projector augmented-wave method. *Physical Review B* **59**, 1758-1775 (1999).
64 Perdew, J. P., Burke, K. & Ernzerhof, M. Generalized Gradient Approximation Made Simple. *Physical Review Letters* **77**, 3865-3868 (1996).
65 Gautier, S., Steinmann, S. N., Michel, C., Fleurat-Lessard, P. & Sautet, P. Molecular adsorption at Pt(111). How accurate are DFT functionals? *Physical Chemistry Chemical Physics* **17**, 28921-28930 (2015).
66 Mathew, K., Sundararaman, R., Letchworth-Weaver, K., Arias, T. A. & Hennig, R. G. Implicit solvation model for density-functional study of nanocrystal surfaces and reaction pathways. *The Journal of Chemical Physics* **140** (2014).
67 Mathew, K., Kolluru, V. S. C., Mula, S., Steinmann, S. N. & Hennig, R. G. Implicit self-consistent electrolyte model in plane-wave density-functional theory. *The Journal of Chemical Physics* **151** (2019).
68 Nelson, R. *et al.* LOBSTER: Local orbital projections, atomic charges, and chemical-bonding analysis from projector-augmented-wave-based density-functional theory. *Journal of Computational Chemistry* **41**, 1931-1940 (2020).
69 Kumari, S. *et al.* Electrocatalytic Hydrogen Evolution at Full Atomic Utilization over ITO-Supported Sub-nano-Ptn Clusters: High, Size-Dependent Activity Controlled by Fluxional Pt Hydride Species. *Journal of the American Chemical Society* **145**, 5834-5845 (2023).
70 Kumari, S. & Sautet, P. Elucidation of the Active Site for the Oxygen Evolution Reaction on a Single Pt Atom Supported on Indium Tin Oxide. *The Journal of Physical Chemistry Letters* **14**, 2635-2643 (2023).

Acknowledgement

The experimental part of this work was supported by Director, Office of Science, Office of Basic Energy Sciences, Chemical Sciences, Geosciences, & Biosciences Division, of the U.S. Department of Energy under Contract DE-AC02-05CH11231, FWP CH030201 (Catalysis Research Program). This research used resources of the Advanced Light Source, a DOE Office of Science User Facility under contract no. DE-AC02-05-CH11231. SEM and 4D-STEM were performed at the Molecular Foundry, supported by the DOE Office of Basic Energy Sciences under the same contract number. The authors want to thank Diamond Light Source for access to beamline B07 (SI35104), which contributed to the results presented here. We want to thank Oleg Kostko from beamline 9.0.1 of the Advanced Light Source for his help with setting up *in situ* XAS measurements. The Solid-Liquid Interface Manipulator (SLIM) arm employed at beamline 9.0.1 of the ALS was financed by the DOE, Office of Science, Office of Basic Energy Sciences, Materials Sciences and Engineering Division, Unlocking Chemical Circularity in Recycling by Controlling Polymer Reactivity across Scales program under the contract no. DE-AC02-05-CH11231, the 23-ID-2 (IOS). M.J. and M.B.S. acknowledge the support by the U.S. Department of Energy, Office of Science. For the simulation part Y.G. and P.S acknowledge support from the National Science Foundation award 2140374. and R.M.K. and P.S. thank the University of California Office of the

President, The National Laboratory Research Fees Program for the award L22CR4468, which supports the Center for Direct Conversion of Captured CO_2 into Chemicals and Fuels. We acknowledge Dr. Yujian Xia, and Dr. Tianying Liu for their kind assistance to our beamline experiments.

Authors Contributions

Y.S., M.J. and J.F. conceived and designed the project under the guidance of M.B.S. and P.Y. Y.S. synthesized the materials and carried out the *in situ* SEIRAS studies with assistance from T.W. M.F.G and A.S. Y.S., M.J. and J.F. performed in situ XAS measurements at the Advanced Light Source and analyzed the data with assistance from L.J., J.L., H.D., S.N. X.Z. and J.G. M.J. and J.F. additionally conducted and analyzed *in situ* XAS measurements at Diamond Light Source. Y.G., R.M.K. and P.S. carried out the DFT calculations. All authors contributed to the discussion of results and to the preparation of the manuscript.

Competing Interests

The authors declare no competing interests.

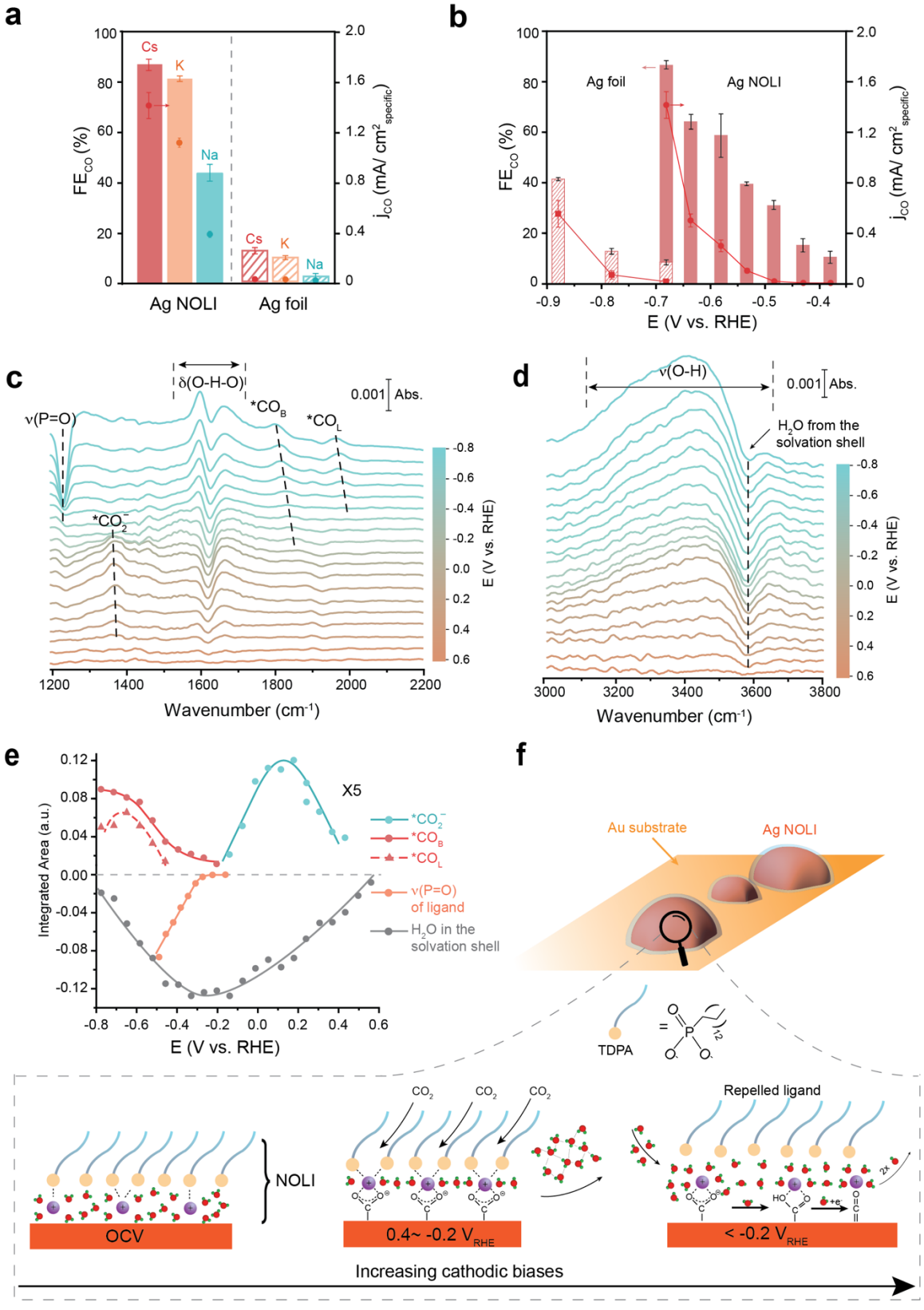

Fig. 1. CO_2 adsorption at low overpotential. a, Comparison of CO FE and partial current density between Ag NOLI and Ag foil, measured at –0.68 V_{RHE} in CO_2-saturated 0.1 M $CsHCO_3$, 0.1M $KHCO_3$ and 0.1 M $NaHCO_3$ electrolytes. **b**,

CO FE and partial current density as a function of applied potential for Ag NOLI and Ag foil, both tested in CO_2-saturated 0.1 M $CsHCO_3$. Error bars in **a** and **b** are one standard deviation of at least three independent measurements. **c–d**, *In situ* ATR-SEIRAS spectra collected from 1200–2200 cm^{-1} (**c**) and 3000–3800 cm^{-1} (**d**) regions for Ag NOLI. Spectra were acquired under applied potentials ranging from 0.6 V_{RHE} to –0.8 V_{RHE} in CO_2-bubbled 0.1 M $CsHCO_3$, referenced to a spectrum collected at 0.6 V_{RHE}. **e**, Integrated absorbance of interfacial species identified in panels **c** and **d** as a function of potential. Positive areas are magnified fivefold for clarity. **f**, A schematic of interfacial processes occurring at different biases for Ag NOLI. The TDPA ligand is depicted as a light-yellow ball (phosphonic acid headgroup) linked to a cyan chain (14-carbon alkyl chain). Cs^+ ions are shown as purple spheres with a central plus sign. Water molecules are represented by a red sphere (oxygen) and two green spheres (hydrogen). For clarity, species outside the ligand layer and minor components (e.g., anions) are omitted.

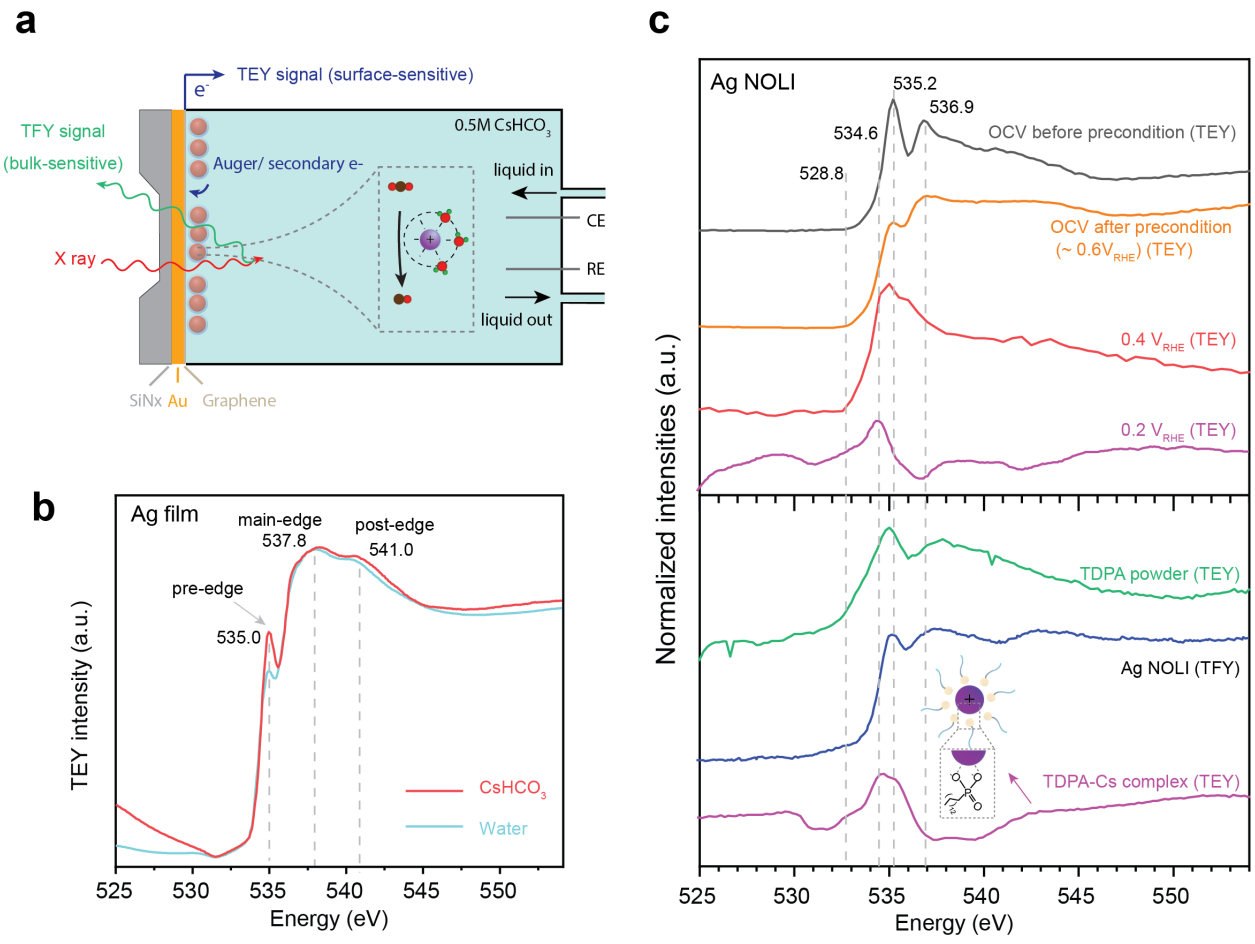

Fig. 2: O K-edge spectra measured by TEY-XAS. **a**, Schematic of the custom-built liquid flow X-ray cell. A silicon nitride window is coated with thin layers of chromium and gold to ensure good electrical conductivity. Three layers of graphene are subsequently deposited onto the gold to prevent electronic interference from the metal substrate. The catalyst is then drop-cast or coated onto the graphene surface. Measurements are performed under continuous liquid flow, with a 3 M Ag/AgCl electrode and a platinum wire serving as the reference and counter electrodes, respectively. **b–c**, Electron yield O K-edge spectra of (**b**) Ag film in H_2O and CO_2-saturated 0.5 M $CsHCO_3$, (**c**) Ag NOLI at different applied potentials in CO_2-saturated 0.5 M $CsHCO_3$, and reference samples. The reference spectra include TDPA powder (green trace) and Cs–TDPA complexes dissolved in ethanol (red trace, with solvent background subtracted).

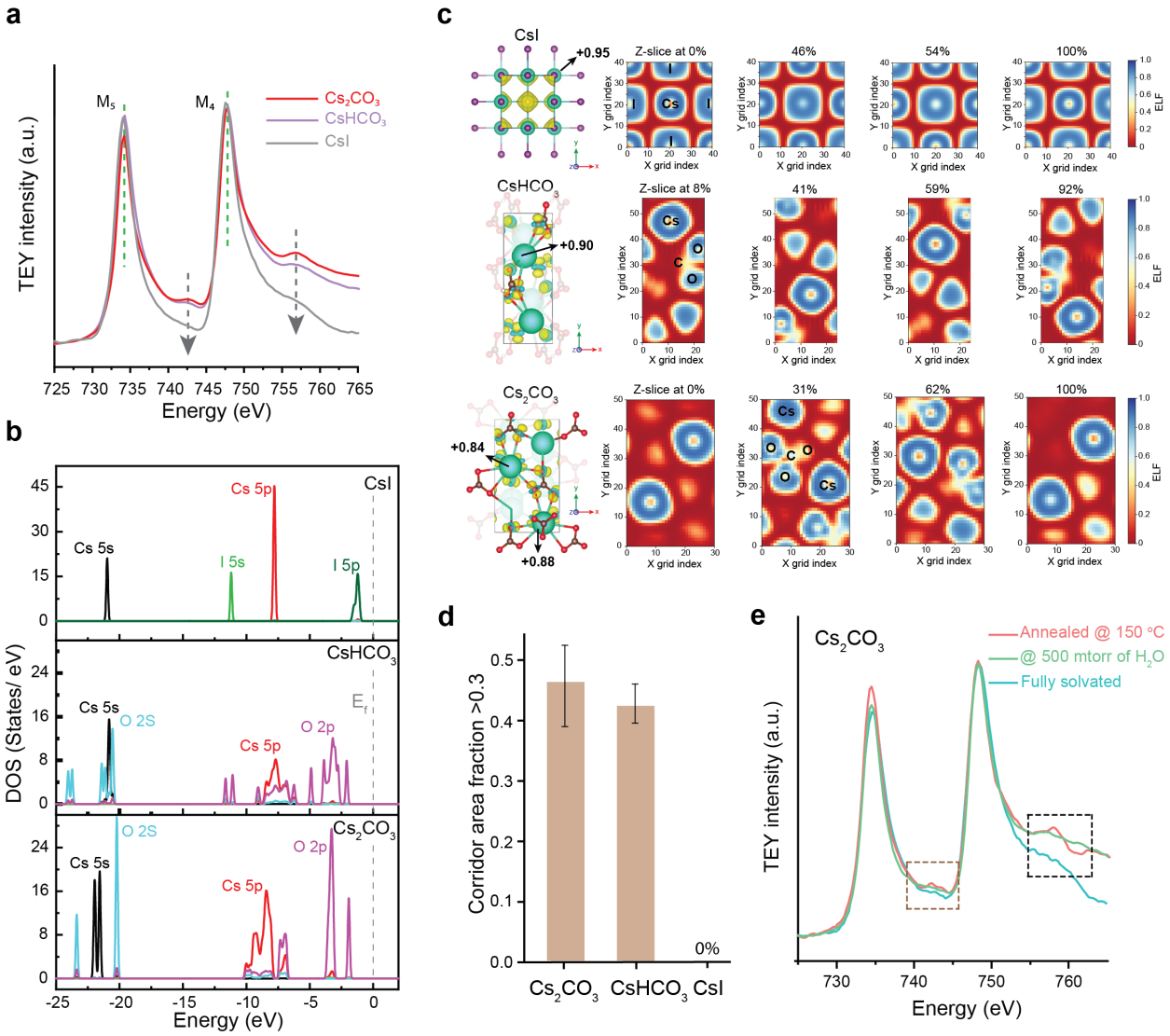

Fig. 3. Cs M-edge reference spectra. a, Cs M-edge spectra of solid-state Cs_2CO_3, $CsHCO_3$, and CsI. **b,** Projected density of states (PDOS) highlighting Cs 5s and 5p states and anion valence states: I 5s/5p in CsI (top), and O 2s/2p in $CsHCO_3$ (middle) and Cs_2CO_3 (bottom). The Fermi level is set to 0 eV. Carbonate phases show a significant orbital mixing between Cs 5p and O 2p states, whereas CsI exhibits well separated ionic manifolds. **c**, Left: differential charge density ($\Delta\varrho$ = ϱ_total – $\Sigma\varrho$_atomic) isosurfaces (positive accumulation / negative depletion) superimposed on the crystal structures (view along the x–y plane) for CsI, $CsHCO_3$, and Cs_2CO_3, including Bader charge value on Cs, revealing directional Cs–O polarization absent in Cs–I. Right: corresponding total charge density slices at four representative z positions, illustrating the emergence of intermediate inter-nuclear charge density corridors for Cs–O but not Cs–I. Atom colors: Cs (green), I (purple), O (red), C (brown), H (white). **d**, Corridor area fraction of Cs_2CO_3, $CsHCO_3$, and CsI, **e**, Cs M-edge spectra of Cs_2CO_3 measured under different water concentrations. Regions of 738–746 eV and 754–762 eV are highlighted, reflecting the evolution of satellite features with increasing water content.

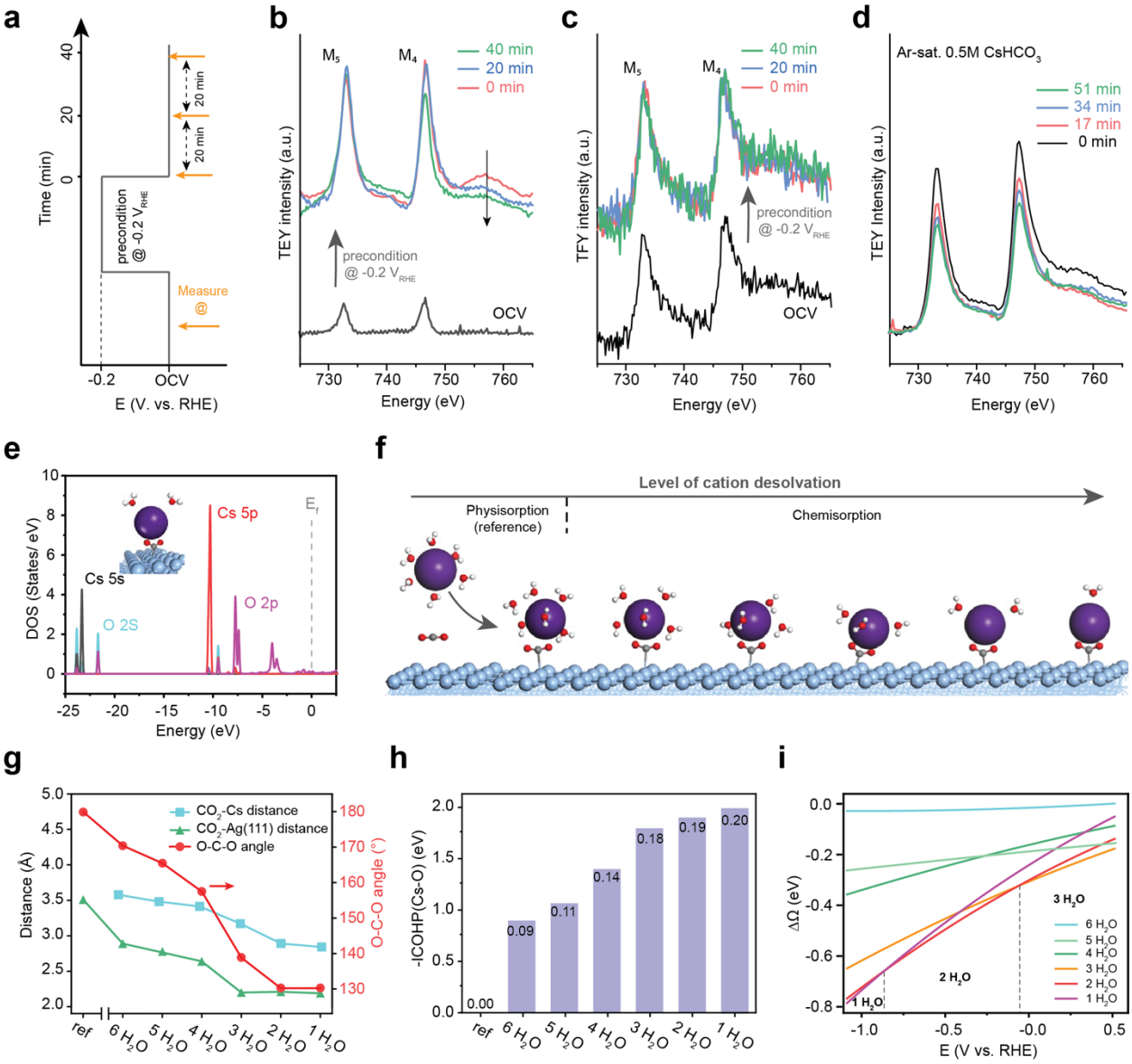

Fig. 4. Cs-*CO_2 interaction probed by *in situ* XAS and DFT calculation. a, Schematic of the experimental protocol. XAS spectra were collected before preconditioning, and at 0 min, 20 min, and 40 min after preconditioning at –0.2 V_{RHE}. **b–c,** *In situ* Cs M-edge spectra acquired in (**b**) total electron yield (TEY) mode and (**c**) total fluorescence yield (TFY) mode in 0.5 M CO_2-saturated $CsHCO_3$., **d**, *in situ* Cs M-edge spectra acquired in TEY mode in 0.5M Ar-saturated $CsHCO_3$. **e**, PDOS of an adsorbed *CO_2 stabilized by a partially desolvated Cs^+; O orbitals are selected exclusively from the two O atoms of adsorbed *CO_2. **f**, GC-DFT-optimized adsorption structures of CO_2 under varying degrees of Cs^+ desolvation. Color code: Cs (purple), O (red), C (gray), H (white). **g,** Structural descriptors including average Cs–O_CO_2 (light blue), Ag (111)–CO_2 (green) bond lengths and the O–C–O bond angle (red) of adsorbed CO_2 across the configurations in **f**. **h,** Negative integrated crystal orbital Hamilton population (–ICOHP) values reflecting the bond strength between Cs and CO_2 in the structures shown in **f**. **i,** Calculated potential-dependent stability of different *CO_2–Cs structures in f with varying degrees of cation desolvation.